Pneumatochemical Impedance Spectroscopy. 1. Principles

Pierre Millet*

Laboratoire de Chimie Inorganique, Université Paris Sud, bâtiment 420, 91405 Orsay cedex, France

Received: June 21, 2005; In Final Form: October 1, 2005

Pneumatochemical impedance spectroscopy (PIS) is the indirect transposition of electrochemical impedance spectroscopy (EIS) to solid−gas reactions. In PIS analysis, an analogy is made between pressure and electrical potential on one hand and gas flow and electric current on the other hand, and pneumatochemical transfer functions are derived from gas-phase measurements. Potentially, this spectroscopy can be used to analyze the dynamics of any solid−gas system including adsorption (surface) and absorption (bulk) phenomena, gas (H_2) permeation across metallic membranes, and electrocatalysis in gaseous fuel cells. Hydrogen absorption by intermetallic compounds (IMCs), a process of great practical interest for hydrogen storage applications, is more specifically considered in this paper, and the kinetic equations derived in this work pertain only to this case. Whereas classical electrochemical impedance measurements are performed using an harmonic analyzer and monochromatic potential (potentiostatic mode) or current (intentiostatic mode) perturbations, PIS investigation of the dynamics of IMC−H_2(g) systems is more conveniently performed using Sievert's-type gas distribution apparatus (SGDA) and polychromatic pressure perturbation signals. This is first because monochromatic isothermal pressure modulations cannot be easily obtained experimentally over the frequency domain of interest and, second, because most IMC−H_2(g) systems exhibit strongly nonlinear behaviors in two-phase domains (hysteresis), and this proscribes harmonic analysis. A further benefit of using SGDA and nonharmonic perturbations is that kinetic and thermodynamic information are collected simultaneously during the same experiment. The measurement and modeling of the pneumatochemical transfer functions associated with IMC−H_2(g) systems, both in solid solution and two-phase domains, are discussed in this paper which is organized in two parts. The principles of PIS analysis, based on the theory of linear and time-invariant systems, are presented in the first part. The dynamics of hydrogen sorption by metals and IMCs is analyzed in the second part, where a detailed analysis of the multistep reaction paths involved in sorption mechanisms is proposed.

1. Introduction

Since the first oil crisis in the early 1970s, political and environmental problems associated with the use of fossil fuels have boosted R&D programs on hydrogen, which potentially can be used as an alternative energy carrier.[1] From a technological viewpoint, hydrogen storage can be adequately obtained by forming metallic hydrides with many elemental metals or intermetallic compounds (IMCs). Reversible hydride-forming IMCs have a long and rich scientific history which started 50 years ago with the discovery of the hydrogen absorption properties of $ZrNi$[2] later followed by those of $LaNi_5$.[3] Since then, a large number of new compounds have been idendified and characterized.[4] Their potentialities for both stationary and mobile applications have attracted increasing interest over the past decades.[5] Practical applications require long term maintenance of large storage capacities and fast reaction rates. This is why numerous hydriding/dehydriding kinetic studies have been published in the literature until recently. From an experimental viewpoint, kinetic experiments are commonly performed either by use of constant hydrogen pressure measurements of the hydrogen flow from a reservoir to a reaction chamber[6] or by measuring the transient pressure in a closed system with constant volume (Sievert's method).[7] Alternative methods including pressure sweeps have also been reported recently.[8] The description of a high-precision, automatic, experimental Sievert's-type gas distribution apparatus (SGDA) can be found in ref 9. In the general sense of acceptance, the word kinetics means the rate (for example expressed in $mol \cdot s^{-1} \cdot g^{-1}$ or in $mol \cdot s^{-1} \cdot cm^{-2}$ when the active surface is known) at which hydrogen is absorbed by (or desorbed from) a given metal or IMC. Rate laws are often expressed as the time-dependent transformed fraction $\alpha(t) = n(t)/n^{max}$, where $n(t)$ is the number of hydrogen moles absorbed at time t ($0 < \alpha < 1$). But kinetic data, when properly analyzed, carry with them detailed information on the multistep reaction mechanism associated with the absorption (desorption) process. General rate laws are interesting for the development of technological applications, but detailed understanding of sorption mechanisms is also needed, first to determine the rate-determing step (rds) of the reaction path and, second, to analyze material degradation under cycling conditions. Analysis of multistep reaction paths is routine in electrochemistry using electrochemical impedance spectroscopy (EIS). Instead of modeling transient current densities produced by any given potential perturbation (time domain analysis), the transfer function of the system is measured (Fourier or frequency domain) using either harmonic[10] or polychromatic perturbations.[11] Transfer functions unambiguously characterize reaction mechanisms and give access to the rate parameter associated with each step. By making an analogy between pressure and electrical potential on one hand and gas flow and electric current on the other hand, it is possible to define the principles of pneumatochemical impedance spectros-

* Phone: 33-1.6915.4812. Fax: 33-1.6915.4754. E-mail: pierre.millet@icmo.u-psud.fr.

10.1021/jp053350m CCC: $30.25
Published on Web 11/24/2005

copy (PIS) which is the indirect transposition of EIS to solid−gas reactions. Whereas typical electrochemical impedance measurements are performed using a harmonic analyzer (monochromatic potential or current perturbations are applied to the system), pneumatochemical impedance measurements are more conveniently performed using a SGDA (nonharmonic perturbations). This is because monochromatic and isothermal pressure modulations cannot be easily obtained experimentally in the frequency domain of interest (heating methods exclude frequency measurements above 1 mHz because of thermal inertia) and because most IMC−H_2(g) systems present strongly nonlinear behavior, evidenced by the presence of a static hysteresis on the isotherms.[12] In a typical Sievert experiment, hydrogen is transferred from a reservoir chamber to a reaction chamber where reaction with the IMC takes place. The driving force to the transfer is an initial pressure difference set between the reservoir and the reactor, and thus, absorption and desorption kinetics are studied in separate experiments. This avoids back and forth displacements along the nonreversible thermodynamic paths observed in the two-phase domains of the isotherms.[11] In that case, the theory of linear and time invariant systems applies and mechanism information can be obtained by analyzing, in the Fourier (frequency) domain, the convolution associated with the pair {pressure; mass flow}. Historically, frequency-domain methods appeared following the pionnering work of Fourier who discovered the properties of mathematical series in his attempt to solve the heat equation.[13] Angstroem was probably the first to report on an experimental method based on Fourier analysis. Using monochromatic temperature perturbations, he determined the thermal conductivity of a metallic rod.[14] The method has then been extensively used along the 20th century in engineering science to analyze the dynamics of various linear systems including electrical and later electrochemical systems. In 1963, Naphthali et al. used the technique to investigate adsorption phenomena for catalysis applications,[15] followed by Yasuda who studied the kinetics of various reactive and diffusive systems.[16] More recently, the hydriding kinetics of IMC from the gas phase has been studied in the frequency domain. Gray et al. proposed to use harmonic perturbations obtained by thermal heating.[17] Then, Millet et al. showed that, using usual SGDA, it was possible to obtain pneumatochemical impedance diagrams similar in shape to those obtained in electrochemical systems using EIS. They were obtained numerically by solving the convolution equation associated with linear and time-invariant systems.[18,19] PIS analysis has therefore a general background. A review of various techniques used to access other nonelectrical transfer functions has been published recently in the literature.[20] The principles and applications of PIS analysis are presented in this paper which is organized in two parts. In the first part, a description of the basic principles of PIS analysis using SGDA is given. The discussion is restricted to gas transfer dynamics with no hydriding reactions. The general characteristics of the pneumatic components found in SGDA are obtained in the time and frequency domains from measurement-supported modeling of transient pressure and gas flow signals. In the second part, the dynamics of hydrogen sorption by metals and IMC is considered in detail.

2. Brief Summary of the Theory of Linear Systems Used in this Paper

In this paper, only time-dependent physical quantities such as pressure and mass flow are considered, and thus, the implicit variable in the following is the time variable t throughout. System theory analyzes the relationships existing between any given input $i(t)$ and the corresponding output $o(t)$. A system is said to be linear and time invariant when the two following conditions are satisfied:

$$\alpha_1 i_1(t) + \alpha_2 i_2(t) \rightarrow \beta_1 o_1(t) + \beta_2 o_2(t) \tag{2.1}$$

where α_1, α_2, β_1, and β_2 are scalars

$$i(t - \tau) \rightarrow o(t - \tau) \tag{2.2}$$

where τ is the time shift.

Let $h(t)$ be the output obtained when the unit impulse (Dirac) function $\delta(t)$ is applied as input. $h(t)$ is called the impulse response

$$\delta(t) \rightarrow h(t) \tag{2.3}$$

It can be shown that for systems satisfying (2.1) and (2.2), the output $o(t)$ is related to the convolution product of the input $i(t)$ by $h(t)$

$$o(t) = \int_{-\infty}^{+\infty} i(\tau)h(t - \tau)\, d\tau = i(t)*h(t) \tag{2.4}$$

Complex exponentials remain frequency unaltered when passing through linear and time-invariant systems. Only amplitude modulations and phase shifts occur. $i(t)$ and $o(t)$ can thus be adequatly expressed on the basis of complex exponentials. This operation is called Fourier transformation

$$G(f) = \mathrm{FT}[g(t)] = \int_{-\infty}^{+\infty} g(t)e^{-j\omega t}\, dt \tag{2.5}$$

where f is the frequency in Hz, $\omega = 2\pi f$ is the pulsation in rad·s^{-1}, and FT[$g(t)$] is the Fourier transform of $g(t)$.

An interesting property of the Fourier transformation is that the convolution product (2.4) in the time (direct) domain is simply an algebraic product in the Fourier (frequency) domain

$$\mathrm{FT}[i(t)*h(t)] = \mathrm{FT}[i(t)]\ \mathrm{FT}[h(t)] = \mathrm{FT}[o(t)] \tag{2.6}$$

The FT of the impulse response $h(t)$ is called the transfer function of the system

$$\mathrm{FT}[h(t)] = H(f) = \int_{-\infty}^{+\infty} h(t)e^{-j\omega t}\, dt \tag{2.7}$$

Thus, for a linear and time-invariant system, the general relationship between input $i(t)$ and output $o(t)$ is a convolution product in the time domain and an algebraic product in the Fourier domain. This system is uniquely described by its transfer function. According to (2.6), the transfer function $H(f)$ can be obtained in principle by taking the ratio of the FTs of any pair $\{i(t); o(t)\}$; i.e., $H(f) = \mathrm{FT}\{o(t)\}/\mathrm{FT}\{i(t)\}$. This is possible as long as the denominator is nonzero at the frequencies of interest. It turns out that many physical systems are linear and time invariant although practical use of (2.4) requires a careful determination of the conditions for which (2.1) and (2.2) are respected. It is the purpose of this paper to show that this is the case for IMC−H_2(g) systems and to show how (2.6) can be used to obtain the corresponding transfer functions from nonharmonic input perturbations. In particular, $H(f)$ transfer functions are obtained from $\{i(t); o(t)\}$ pairs such as {pressure (t); mass flow (t)} signals recorded on SGDAs, thus providing a powerful tool for kinetic analysis to those who use this experimental technique. In the first part of this paper, the

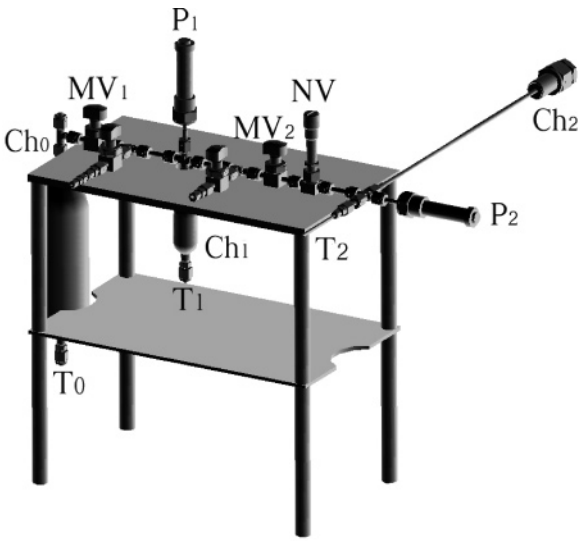

Figure 1. Schematic drawing of the experimental setup (SGDA) used for gas transfer experiments.

discussion is restricted to gas transfer dynamics (with no hydriding reaction).

3. Experimental Section

A schematic drawing of the manual SGDA used to analyze gas transfer dynamics and perform PIS analysis is shown in Figure 1. The system consists of three chambers (Swagelok Co.) interconnected with stainless steel tubing ($^1/_4$ in. internal diameter) and VCR connectors: (i) a reservoir chamber Ch_0 (316L stainless steel double-ended cylinder; $V_{Ch_0} = 986 \pm 1$ cm^3), (ii) a reference volume chamber Ch_1 ($V_{Ch_1} = 60.428 \pm 0.001$ cm^3), and (iii) a reaction chamber Ch_2 (1 in. VCR connector, $V_{Ch_2} = 62.143 \pm 0.001$ cm^3). Ex situ control of the SGDA's average temperature is obtained within ± 0.5 °C using adequately positionned polystyrene-based shields and forced air circulation for room-temperature measurements. Optionally, Ch_2 can be introduced in a furnace for high-temperature measurements up to 350 °C. A fast response chromel−alumel thermocouple T_2 (Thermocoax Co.) is mounted in situ in Ch_2 to measure temperature changes during hydrogen absorption/desorption. Two additional thermocouples (T_0, T_1) can be used for more accurate mass balance measurements.

Four manual diaphragm valves (MVs, Swagelok Co.) are used for gas management and setting of initial gas transfer conditions. A bellows-sealed valve (Swagelok Co.) equipped with a metering stem tip is placed in the circuitry. This "needle valve" (NV) acts as a gas flow regulator allowing nonconvective and isothermal gas transfers from Ch_1 to Ch_2. A six turn micrometer handle allows repeatable flow settings within a range of values manually selected by adjusting an internal lock screw so as to adapt gas flows to gas viscosities. Alternatively, the valve can be replaced by a porous silver-coated nickel filter (Swagelok Co., ca. 0.5 μm average pore diameter) mounted on a VCR connector. Such filters are cheaper than the valves but do not allow adjustable flow settings. They are commonly used in SGDAs to confine the powdered IMC inside the reaction chamber during gas transfers.[9] Two pressure transducers (Keller Co.) $0-3000 \pm 0.2$ mbar with numerical output are used to sample transient pressure signals $P_1(t)$ and $P_2(t)$ during gas transfer experiments. Numerical sampling is achieved using a RS485 serial bus connected to a personnal computer, and sampling rates up to one measurement every 20 ms can be obtained. The test-bench can be air-purged down to secondary vacuum using an air-cooled diffusion pump (from Alcatel Co.). In a typical experiment, Ch_1 is initially pressurized at P_1^0 (using gas stored in Ch_0) and Ch_2 at P_2^0. Then, MV_1 and MV_2 are closed until pressure and temperature equilibrium is obtained in Ch_1 and Ch_2. Finally, MV_2 is opened. The gas in Ch_1 expands rapidly into the tubing section between MV_2 and NV (1.320 cm^3; a few mbar drop is observed on P_1). Then the gas is transferred from Ch_1 ($V_1 = V_{Ch_1} + 1.320$ cm^3) to Ch_2 ($V_2 = V_{Ch_2} - 1.320$ cm^3) through the NV which acts as a gas flow regulator. Pressure equilibrium in both Ch_1 and Ch_2 is reached more or less rapidly, depending on the position of the micrometer handles. Alphagaz grade 1 gases (H_2 and Ar) are used in the experiments.

4. Time Domain Analysis of Gas Transfer Dynamics

Calibration measurements of the NV are made in both direct and reverse directions, by transferring the gas (H_2 or Ar) between Ch_1 and Ch_2. Initial pressure differences $P_1^0 - P_2^0$ are set between the two chambers, and transient pressure signals are sampled until equilibrium is reached. Model equations are derived from Poiseuille's law and used to fit experimental data.

4.1. Poiseuille's Law. Gas flow across the needle valve is known to follow Poiseuille's law.[21] Poiseuille determined in 1844 the empirical relationship which relates the volumic flow of liquids in tubes of circular sections to the pressure drop at end sides. When applied to gas transfers, this relationship is written as

$$\frac{dV}{dt}(t) = \frac{([P_1(t)]^2 - [P_2(t)]^2)\pi r^4}{16\eta P_0 L} \tag{4.1}$$

where V is the volume of gas of viscosity η transferred at pressure P_0 along a tube of length L and radius r. Assuming that the gas behaves ideally (this is justified for systems with plateau pressure values up to a few bars as those considered here), (4.1) can be written as

$$\frac{dn}{dt}(t) = \frac{K_V}{RT}([P_1(t)]^2 - [P_2(t)]^2) \tag{4.2}$$

$$K_V = \frac{\pi r^4}{16\eta L} \quad \mathrm{m^3 \cdot Pa^{-1} \cdot s^{-1}} \tag{4.3}$$

is a constant which charaterizes the needle valve and the gas.

4.2. Modeling of Gas Transfer Dynamics. 4.2.1. Model Equations. Conservation of mass during gas transfer requires that the hydrogen molar flow has a constant value at different points in the pneumatic circuit

$$-\left(\frac{dn}{dt}\right)_{V_1} = +\left(\frac{dn}{dt}\right)_{NV} = +\left(\frac{dn}{dt}\right)_{V_2} \tag{4.4}$$

For an ideal gas, the pressure change in Ch_1 is

$$\frac{dP_1(t)}{dt} = \frac{RT}{V_1}\frac{dn}{dt}(t) \tag{4.5}$$

Thus, when the gas is transferred from Ch_1 to Ch_2

$$\frac{dP_1}{dt} = -\frac{K_V}{V_1}[P_1^2(t) - P_2^2(t)] \tag{4.6}$$

$$\frac{dP_2}{dt} = \frac{K_V}{V_2}[P_1^2(t) - P_2^2(t)] \tag{4.7}$$

Pressure transients $P_1(t)$ and $P_2(t)$ are solutions of the system of differential eqs 4.6 and 4.7 which can be solved by using the appropriate initial and boundary conditions:

Initial Conditions.

$$P_1(t{=}0) = P_1^{\,0} \quad P_2(t{=}0) = P_2^{\,0} \quad \frac{dn}{dt}(t{<}0) = 0 \quad (4.8)$$

At $t = 0$, the manual valve MV_2 is wide open and gas transfer proceeds. $dn/dt(t)$ is maximum at $t = 0$ and then decreases steadily down to zero when the pressures reach a common equilibrium value in each volume chamber.

Boundary Conditions. Mass conservation during gas transfer requires that

$$n_1(t) + n_2(t) = n_T = \frac{P_1(t)V_1}{RT} + \frac{P_2(t)V_2}{RT} \quad (4.9)$$

4.2.2. Analytical Solutions. Integration of the system of differential eq 4.6 and eq 4.7 using initial eq 4.8 and boundary eq 4.9 conditions yields analytical expressions for $P_1(t)$, $P_2(t)$, $\Delta P(t) = P_1(t) - P_2(t)$ and $dn/dt(t)$ as a function of the different parameters of the system (K_V, V_1, V_2, P_1^0, P_2^0)

$$\text{Setting } \alpha = +2K_V\left[\frac{P_1^{\,0}}{V_2} + \frac{P_2^{\,0}}{V_1}\right] \quad (4.10)$$

expressions 4.11−4.14 are obtained.

4.2.3. Comparison with Experimental Results. Figure 2 shows the results of a typical gas (H_2) transfer experiment obtained with the experimental setup of Figure 1. The experimental H_2 molar flow dn/dt is not directly measured but obtained from $P_1(t)$ using eq 4.5. Experimental data are fitted using K_V as unique adjustable parameter.

Using the same procedure, K_V can be determined for different positions of the micrometer handles on the valve and different gases (Figure 3). Above five divisions, deviations from Poiseuille's law are observed and nonisothermal gas transfers occur.

4.3. Linearization of Poiseuille's Formula. Poiseuille's formula (4.2), which relates molar gas flow to pressure drops across needle valves and filters, is a nonlinear relation. This is why the use of electrical analogies for the modeling of pneumatic circuits is not straightforward. Since Fourier-domain modeling requires linear and time invariant systems (as discussed above in section 2), it is necessary to determine the conditions for which (4.2) can be linearized, i.e., for which $dn/dt(t)$ becomes a linear function of the simple pressure difference $\Delta P(t) = [P_1(t) - P_2(t)]$. This is obtained in two different experimental situations:

First, when $V_1 = V_2$, (4.14) simplifies into

$$\frac{dn}{dt}(t) = (P_1^{\,0} + P_2^{\,0})\frac{K_V}{RT}\Delta P(t) \quad (4.15)$$

when $P_2^{\,0} \neq 0$

$$\frac{dn}{dt}(t) = P_1^{\,0}\frac{K_V}{RT}\Delta P(t) \quad (4.16)$$

when $P_2^{\,0} = 0$

Second, in the general case when $V_1 \neq V_2$, linearity is approached when $\Delta P(t)$ is small (the extend to which $\Delta P°$ must be small depends on the extend to which V_1/V_2 differs from unity). Since $\Delta P(t)$ is maximum at $t = 0$, this condition can be rewritten $\Delta P°$ is small. In that case

$$[P_1^{\,2}(t) - P_2^{\,2}(t)] = [P_1(t) - P_2(t)][P_1(t) + P_2(t)] \approx (P_1^{\,0} + P_2^{\,0})\,\Delta P(t) \quad (4.17)$$

These two conditions are precisely those used experimentally to analyze the dynamics of IMC−H_2(g) systems. $V_1 \approx V_2$ is required to obtain the highest precision in pressure measurements during gas transfers and a small value for $\Delta P°$ is required to ensure quasi-isothermal gas transfers. For example, in the experimental setup of Figure 1, $V_1/V_2 = 0.985$. Using $\Delta P° =$

$$P_1(t) = \frac{(V_1P_1^{\,0} + V_2P_2^{\,0})}{(V_1 - V_2)}\left[\frac{1 + \dfrac{(P_1^{\,0} + P_2^{\,0})}{(P_1^{\,0} - P_2^{\,0})}e^{\alpha t}}{1 + \dfrac{(V_1 + V_2)(P_1^{\,0} + P_2^{\,0})}{(V_1 - V_2)(P_1^{\,0} - P_2^{\,0})}e^{\alpha t}}\right] \quad (4.11)$$

$$P_2(t) = \frac{V_1}{V_2}[P_1^{\,0} - P_1(t)] + P_2^{\,0} = \frac{V_1}{V_2}\left[P_1^{\,0} - \frac{(V_1P_1^{\,0} + V_2P_2^{\,0})}{(V_1 - V_2)}\left[\frac{1 + \dfrac{(P_1^{\,0} + P_2^{\,0})}{(P_1^{\,0} - P_2^{\,0})}e^{\alpha t}}{1 + \dfrac{(V_1 + V_2)(P_1^{\,0} + P_2^{\,0})}{(V_1 - V_2)(P_1^{\,0} - P_2^{\,0})}e^{\alpha}t}\right]\right] + P_2^{\,0} \quad (4.12)$$

$$\Delta P(t) = P_1(t) - P_2(t) = P_1(t)\left[1 + \frac{V_1}{V_2}\right] - \frac{V_1}{V_2}P_1^{\,0} - P_2^{\,0} = \frac{(V_1 + V_2)}{V_2}\frac{(V_1P_1^{\,0} + V_2P_2^{\,0})}{(V_1 - V_2)}\left[\frac{1 + \dfrac{(P_1^{\,0} + P_2^{\,0})}{(P_1^{\,0} - P_2^{\,0})}e^{\alpha t}}{1 + \dfrac{(V_1 + V_2)(P_1^{\,0} + P_2^{\,0})}{(V_1 - V_2)(P_1^{\,0} - P_2^{\,0})}e^{\alpha t}}\right] - \frac{V_1}{V_2}P_1^{\,0} - P_2^{\,0} \quad (4.13)$$

$$\frac{dn}{dt}(t) = +\frac{4K_V}{RT}\frac{(V_1P_1^{\,0} + V_2P_2^{\,0})^2}{(V_1 - V_2)^2}\frac{(P_1^{\,0} + P_2^{\,0})}{(P_1^{\,0} - P_2^{\,0})}\left[\frac{e^{\alpha t}}{\left(1 + \dfrac{(V_1 + V_2)}{(V_1 - V_2)}\dfrac{(P_1^{\,0} + P_2^{\,0})}{(P_1^{\,0} - P_2^{\,0})}e^{\alpha t}\right)^2}\right] \quad (4.14)$$

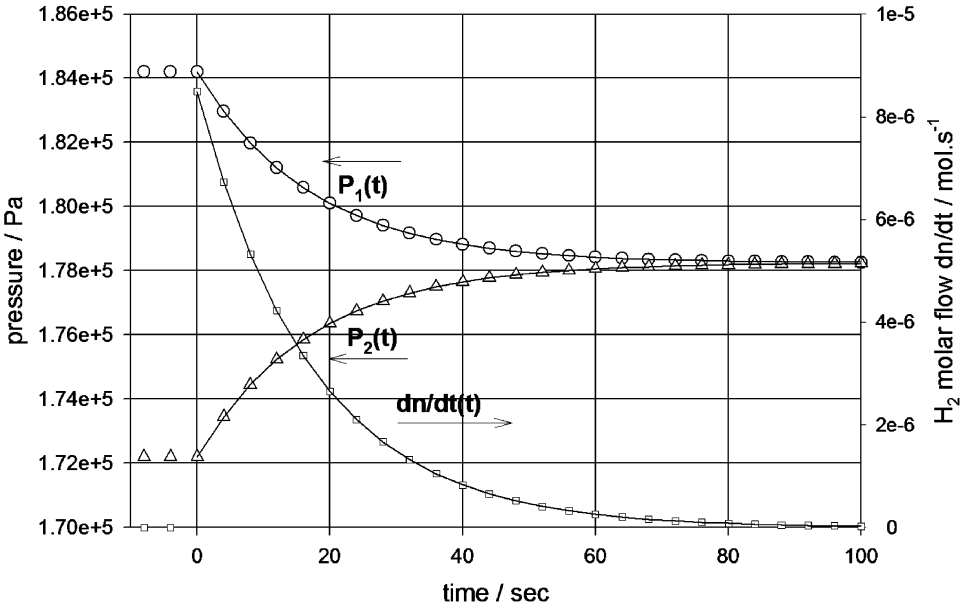

Figure 2. Typical experimental (symbols) transient pressures, $P_1(t)$ and $P_2(t)$, and molar H_2 flow $dn/dt(t)$ obtained using the experimental setup of Figure 1, and their fits using model equations (4.11), (4.12), and (4.14). $V_1 = 61.748$ cm^3; $V_2 = 60.823$ cm^3; $T = 303$ K; $P_1^0 = 1.842 \times 10^5$ Pa; $P_2^0 = 1.722 \times 10^5$ Pa; $\Delta P^\circ = 0.120 \times 10^5$ Pa; $K_V = 5.0 \times 10^{-12}$ m^3·Pa^{-1}·s^{-1}.

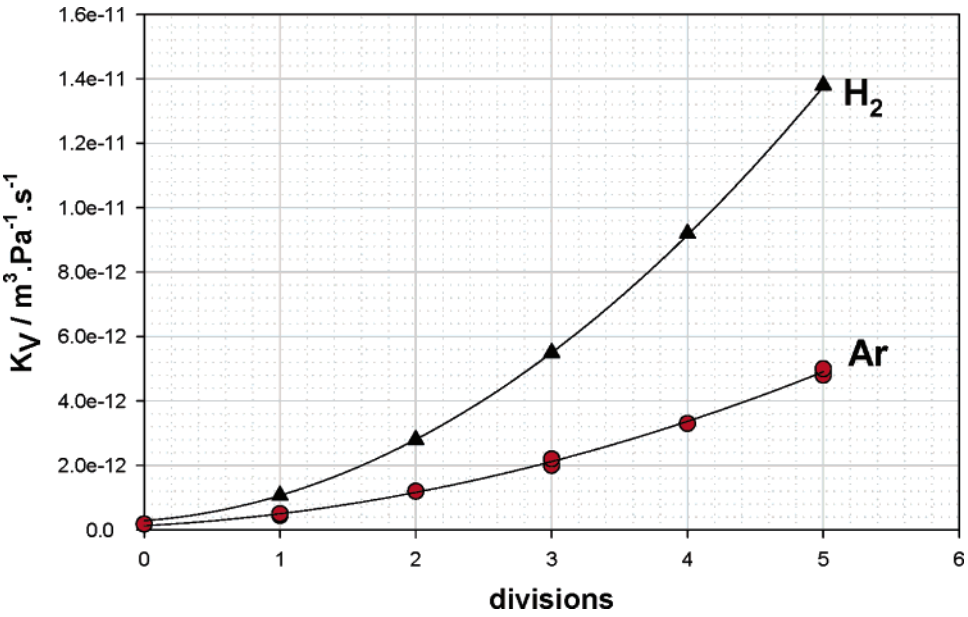

Figure 3. Calibration of the needle valve: plots of the valve constant K_V as a function of the position of the micrometric handle for hydrogen and argon at room temperature.

120 mbar, the linear approximation is satisfied up to 99%. In the following, we will assume that the needle valve behaves linearly, even for cases when $V_1 \neq V_2$, as long as the initial difference of pressure remains sufficiently small (typically lower than 0.5 bar), a condition easily satisfied experimentally.

5. Power Spectral Density and Practical Sampling

Analytical FTs of eqs 4.11 to 4.14 are derived in the Appendix. The series in the real and imaginary parts of expressions A-1 to A-4 come from a series approximation of the exponential function during integration. In practice, convergence is obtained rapidly for $n < 100$. Expressions A-1 to A-4 can be used to determine the Nyquist frequency f_c at which the transient signals must be sampled to avoid under-sampling-related effects in the Fourier domain.[22] A correct sampling is a key factor for obtaining experimental transfer functions. The sampling rate must respect the Nyquist criterion which states that the signal must be sampled more than twice as fast as the highest waveform frequency (f_c). If not, it turns out that all of the power spectral density which lies outside of the frequency range $-f_c < f < f_c$ is spuriously moved into that range and the spectrum is corrupted. This phenomenon is called aliasing.[22] The problem is exemplified in Figure 4 where the power spectral density (PSD, defined by (5.1)) of the hydrogen mass flow $dn/dt(t)$ in Figure 2 is plotted as a function of frequency.

$$\mathrm{PSD}(dn/dt) = \sqrt{\mathrm{Re}\{dn/dt(\omega)\}^2 + \mathrm{Im}\{dn/dt(\omega)\}^2} \quad (5.1)$$

The discrete Fourier transform (DFT, ref 22) of the experimental $dn/dt(t)$ in Figure 2 is computed for different sampling rates and compared to the analytical, uncorrupted spectrum of (A-4).

The numerical PSD becomes extremely noisy at frequencies higher that the Nyquist criterion. Aliasing effects appear in the

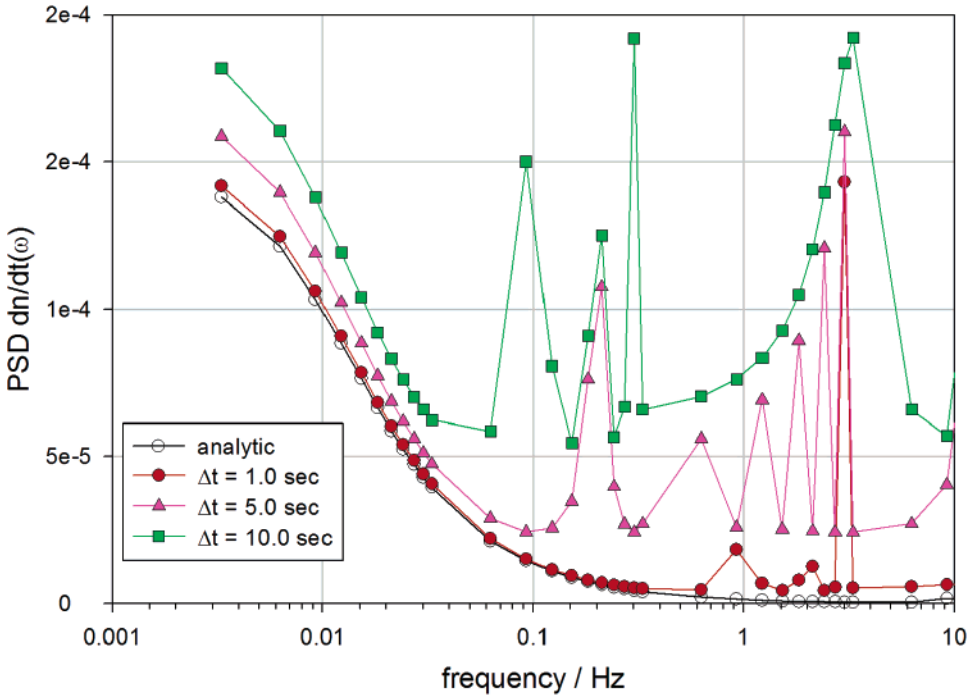

Figure 4. Experimental PSD of the H_2 molar gas flow dn/dt in Figure 2 calculated by DFT for different acquisition rates (symbols) and analytical PSD (from A4).

low-frequency domain as the sampling rate is decreased. The power which lies outside $\pm f_c = \pm 1/(2\Delta t)$ is moved into the range $-f_c < f < +f_c$. In other words, high-frequency components of a time function can impersonate low frequencies if the sampling rate is too low. In a typical experiment, a correct sampling rate requires at least one measurepoint per second until pressure equilibrium is reached.

6. Fourier Domain Analysis of Gas Transfer Dynamics: Pneumatic Transfer Functions

By using the convolution eq 2.4 in the Fourier domain (2.6), it is potentially possible to measure the pneumatic transfer function of the SGDA used for the experiments, as long as the linearization conditions discussed in section 4.3 are applicable. The transfer functions of particular interest are those which relate pressure perturbations to the gas flow responses (flow/force relationship):

$$Z_1(\omega) = \frac{P_1(\omega)}{\mathrm{d}n/\mathrm{d}t(\omega)} \tag{6.1}$$

pneumatic impedance of reservoir chamber Ch_1

$$Z_2(\omega) = \frac{P_2(\omega)}{\mathrm{d}n/\mathrm{d}t(\omega)} \tag{6.2}$$

pneumatic impedance of reaction chamber Ch_2

$$Z_V(\omega) = \frac{(P_1 - P_2)(\omega)}{\mathrm{d}n/\mathrm{d}t(\omega)} \tag{6.3}$$

pneumatic impedance of needle valve NV

6.1. Analytical Pneumatic Transfer Functions. Analytical transfer functions can be obtained in the general (nonlinear) case when $V_1 \neq V_2$ and $P_2^0 \neq 0$ using definitions (6.1), (6.2), and (6.3) and invidual FTs (A-1), (A-2), and (A-3). A detailed analysis of the graphs of $Z_1(\omega)$, $Z_2(\omega)$, and $Z_3(\omega)$ obtained in this general case is nontrivial because of nonlinearities. This is beyond the scope of this paper. Simpler analytical expressions are obtained by considering the linear case when $V_1 \approx V_2 = V$ (this is the case for the SGDA used in this work) and $P_2^0 = 0$ (by considering the transient part of $P_1(t)$ and $P_2(t)$ in Figure 2). In that case, (A-1), (A-2), and (A-3) can be simplified and the transfer functions written as

$$Z_1(\omega) = \frac{RT}{K_V P_1^{\,0}} - j\frac{1}{\omega}\left[\frac{RT}{V}\right] \tag{6.4}$$

$$Z_2(\omega) = -j\frac{1}{\omega}\left[\frac{RT}{V}\right] \tag{6.5}$$

$$Z_3(\omega) = \frac{RT}{K_V P_1^{\,0}} \tag{6.6}$$

The graphs of $Z_1(\omega)$, $Z_2(\omega)$, and $Z_3(\omega)$ from (6.4), (6.5), and (6.6) are schematically plotted in Figure 5 in Nyquist coordinates.

$$\text{Setting: } \begin{cases} R_V = \dfrac{RT}{K_V P_1^{\,0}} \equiv \text{Pa·s·mol}^{-1} \\ C = \dfrac{V}{RT} \equiv \text{mol·Pa}^{-1} \end{cases} \tag{6.7}$$

$Z_1(\omega)$, $Z_2(\omega)$, and $Z_3(\omega)$ can then be rewritten

$$Z_1(\omega) = R_V - j\frac{1}{\omega C} \tag{6.8}$$

$$Z_2(\omega) = -j\frac{1}{\omega C} \tag{6.9}$$

$$Z_3(\omega) = R_V \tag{6.10}$$

Equation 6.8 is the impedance expression for the series connection of a resistance and a capacitor. The high-frequency value on the real axis is the pneumatic resistance associated with the needle valve. Because of gas compressibility, eq 6.7 is a function of the boundary value P_1^0. The higher the pressure

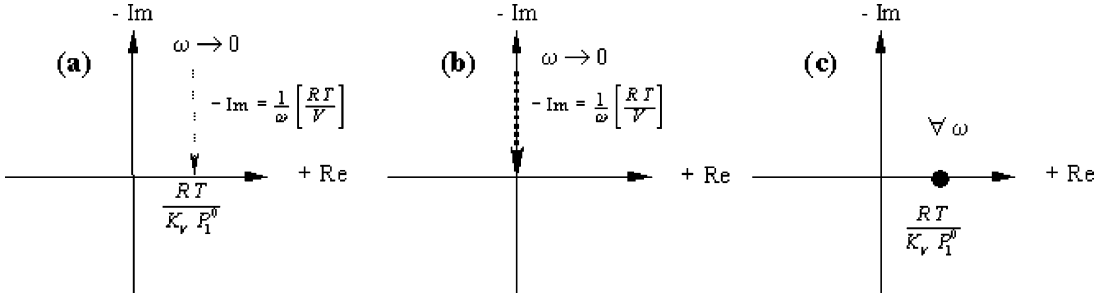

Figure 5. Schematic graph of the pneumatic impedances obtained when $V_1 = V_2$ and $P_2^0 = 0$: (a) $Z_1(\omega)$, (b) $Z_2(\omega)$, (c) $Z_3(\omega)$.

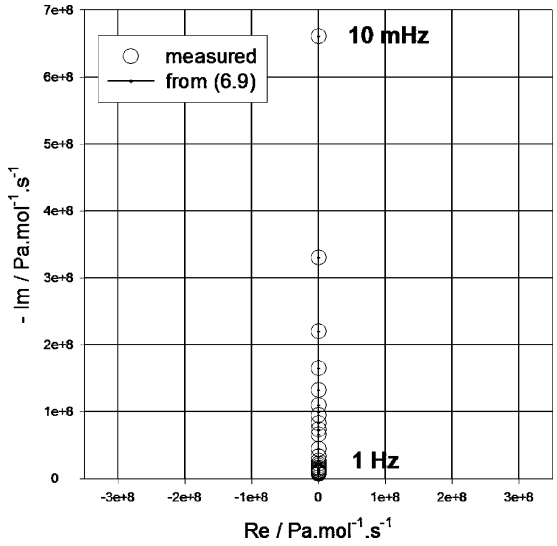

Figure 6. Impedance diagram of the reaction chamber in Nyquist coordinates.

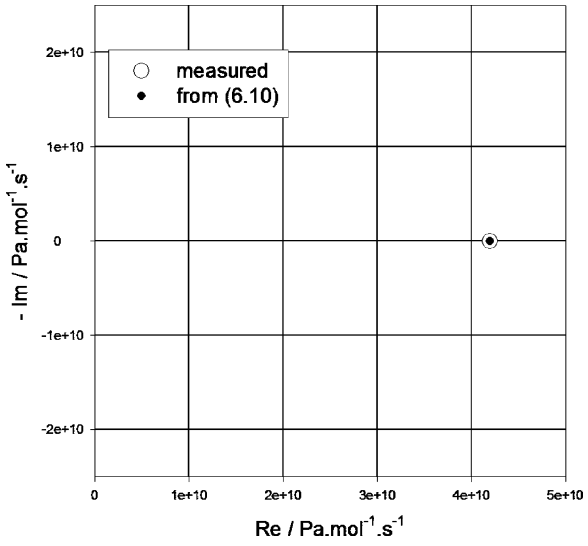

Figure 7. Impedance diagram of the needle valve in Nyquist coordinates.

of transfer, the higher the gas flow is and, thus, the lower the pneumatic resistance. The low-frequency behavior is that of a capacitor, the capacitance of which is related to the volume of the volumic chambers (V) through (6.7). Equation 6.9 is the impedance of a pure capacitance related to V, the volume of the reaction chamber. Finally, (6.10) is the expression of the impedance of a pure resistance, the pneumatic impedance associated with needle valve. The corresponding graph in Nyquist coordinates is a point on the real axis, independent of the pulsation ω.

6.2. Experimental Pneumatic Transfer Functions. In the experiment of Figure 2, V_1 is close to V_2 ($V_1/V_2 = 0.985$) and $\Delta P°$ is small (120 mbar). Thus, the NV has a linear behavior. Experimental impedance diagrams for $Z_1(\omega)$, $Z_2(\omega)$, and $Z_3(\omega)$ can be obtained from adequately sampled transient pressures and gas flow signals using (2.6).

Figure 6 shows the experimental pneumatic transfer function of the reaction chamber Ch_2 in Nyquist coordinates and the calculated values obtained from eq 6.9. The semiline localized in the {+Re; −Im} complex plan is characteristic of a capacitor, as discussed in section 6.1. The frequency dependence of the imaginary part yields a constant volume value V according to (6.7), which is the exact value of V_2 in the experimental setup of Figure 1. Figure 7 shows the experimental and calculated (6.7) pneumatic transfer function of the needle valve in Nyquist coordinates. This is a point on the real axis, independent of frequency, charateristic of a pure resistance as shown by (6.7). Other gas transfer experiments at higher initial pressures (not represented here) yield lower resistance values and vice versa at lower initial pressures, as predicted by (6.7).

5. Conclusions

The dynamics of gas transfer in SGDAs is analyzed in the case where no IMC is placed in the reaction chamber. It is shown that gas transfers between the reference and the (empty) reaction chambers follow Poiseuille's law. Analytical expressions of the transient pressures and molar gas flow are derived by integrating Poiseuille's law and used to fit experimental data. Calculated transients are found in close agreement with measurements, and the valve is calibrated for different positions of the micrometer handles and two different gases. The spectral densities of these transients are then calculated and compared to analytical transforms. It is shown that in a typical experiment, a sampling rate of at least one measurement point per second is required to avoid under-sampling-related problems such as aliasing. By use of the convolution equation (2.6) in the Fourier domain, analytical expressions of pneumatic impedances can be obtained. It is shown that Poiseuille's law can be linearized either by using reference and reaction chambers of similar volumes (4.15 and 4.16) or by setting small initial pressure differences $P_1^0 - P_2^0$ (4.17). In such cases, the needle valve acts as a pneumatic resistance, the value of which (6.7) is independent of the pulsation ω. The reservoir and reactions chambers act as pneumatic capacitors, the capacitances of which (6.7) are related to the volume of the two chambers. It is therefore possible to model pneumatic circuits such as SGDAs using linear electrical analogies. This simplification can be used to analyze the dynamics of hydrogen sorption by IMC, as discussed in part 2 of this series.

Acknowledgment. Financial support from Compagnie Européenne des Technologies de l'Hydrogène, Ecole Polytechnique, Palaiseau, France is gratefully acknowledged.

Appendix: Derivation of Analytical FTs in the General Case ($V_1 \neq V_2$ and $P_0^2 \neq 0$)

1. Fourier Transform of $P_1(t)$. From (4.11), $P_1(t)$ can be written as

$$P_1(t) = K\left[\frac{1 + Ae^{\alpha t}}{1 + Be^{\alpha t}}\right]$$

$P_1(s)$, the Laplace transform of $P_1(t)$, is obtained by direct integration using the series approximation

$$\frac{1}{1 + \frac{1}{B}e^{-\alpha}} = \sum_{n=0}^{\infty}\left(-\frac{1}{B}e^{-\alpha t}\right)^n$$

where $x^0 = 0\ \forall\ x \in R$. This yields

$$\frac{P_1(s)}{K} = \frac{A}{B}\sum_{n=0}^{\infty}\left(\frac{-1}{B}\right)^n\left(\frac{1}{s + n\alpha}\right) + \frac{1}{B}\sum_{n=0}^{\infty}\left(\frac{-1}{B}\right)^n\frac{1}{s + (n+1)\alpha}$$

The Fourier transform $\mathrm{TF}\{P_1(t)\} = P_1(\omega)$ is obtained for $s = j\omega$ after determining K, A, and B

$$P_1(j\omega) = \left(\frac{V_1P_1^{\,0} + V_2P_2^{\,0}}{V_1 + V_2}\right)\left[\sum_{n=0}^{\infty}\left(-\frac{(V_1 - V_2)}{(V_1 + V_2)}\frac{(P_1^{\,0} - P_2^{\,0})}{(P_1^{\,0} + P_2^{\,0})}\right)^n\left(\frac{n\alpha}{n^2\alpha^2 + \omega^2}\right) + \left(\frac{P_1^{\,0} - P_2^{\,0}}{P_1^{\,0} + P_2^{\,0}}\right)\sum_{n=0}^{\infty}\left(-\frac{(V_1 - V_2)}{(V_1 + V_2)}\frac{(P_1^{\,0} - P_2^{\,0})}{(P_1^{\,0} + P_2^{\,0})}\right)^n\left(\frac{(n+1)\alpha}{(n+1)^2\alpha^2 + \omega^2}\right) - j\left[\sum_{n=0}^{\infty}\left(-\frac{(V_1 - V_2)}{(V_1 + V_2)}\frac{(P_1^{\,0} - P_2^{\,0})}{(P_1^{\,0} + P_2^{\,0})}\right)^n\left(\frac{\omega}{n^2\alpha^2 + \omega^2}\right) + \left(\frac{P_1^{\,0} - P_2^{\,0}}{P_1^{\,0} + P_2^{\,0}}\right)\sum_{n=0}^{\infty}\left(-\frac{(V_1 - V_2)(P_1^{\,0} - P_2^{\,0})}{(V_1 + V_2)(P_1^{\,0} + P_2^{\,0})}\right)^n\left(\frac{\omega}{(n+1)^2\alpha^2 + \omega^2}\right)\right]\right]$$

renormalization along the y axis requires a Dirac function $\delta(\nu{=}0)$ on the real part and finally

$$\mathrm{TF}\{P_1(t)\} = \mathrm{TL}\{P_1(t), s{=}j\omega\} + \left(\frac{V_1P_1^{\,0} + V_2P_2^{\,0}}{V_1 + V_2}\right)\frac{1}{2}\delta(\nu{=}0) \tag{A1}$$

2. Fourier Transform of $P_2(t)$. From (4-12)

$$P_2(t) = \frac{V_1}{V_2}[P_1^{\,0} - P_1(t)] + P_2^{\,0} \rightarrow P_2(j\omega) = -\frac{V_1}{V_2}P_1(j\omega) - \frac{j}{\omega}\left(\frac{V_1}{V_2}P_1^{\,0} + P_2^{\,0}\right)$$

$P_2(\omega)$ is obtained from $P_1(\omega)$ in (A-1)

$$P_2(j\omega) = -\left(\frac{V_1}{V_2}\right)\frac{(V_1P_1^{\,0} + V_2P_2^{\,0})}{(V_1 + V_2)}\left[\sum_{n=0}^{\infty}\left(-\frac{(V_1 - V_2)}{(V_1 + V_2)}\frac{(P_1^{\,0} - P_2^{\,0})}{(P_1^{\,0} + P_2^{\,0})}\right)^n\left(\frac{n\alpha}{n^2\alpha^2 + \omega^2}\right) + \frac{(P_1^{\,0} - P_2^{\,0})}{(P_1^{\,0} + P_2^{\,0})}\sum_{n=0}^{\infty}\left(-\frac{(V_1 - V_2)}{(V_1 + V_2)}\frac{(P_1^{\,0} - P_2^{\,0})}{(P_1^{\,0} + P_2^{\,0})}\right)^n\left(\frac{(n+1)\alpha}{(n+1)^2\alpha^2 + \omega^2}\right) - j\left[\sum_{n=0}^{\infty}\left(-\frac{(V_1 - V_2)}{(V_1 + V_2)}\frac{(P_1^{\,0} - P_2^{\,0})}{(P_1^{\,0} + P_2^{\,0})}\right)^n\left(\frac{\omega}{n^2\alpha^2 + \omega^2}\right) + \frac{(P_1^{\,0} - P_2^{\,0})}{(P_1^{\,0} + P_2^{\,0})}\sum_{n=0}^{\infty}\left(-\frac{(V_1 - V_2)}{(V_1 + V_2)}\frac{(P_1^{\,0} - P_2^{\,0})}{(P_1^{\,0} + P_2^{\,0})}\right)^n\left(\frac{\omega}{(n+1)^2\alpha^2 + \omega^2}\right)\right] + j\frac{1}{\omega}\frac{(V_1 + V_2)}{V_1}\right]$$

renormalization along the y axis requires a Dirac function $\delta(\nu{=}0)$ on the real part and finally

$$\mathrm{TF}\{P_2(t)\} = \mathrm{TL}\{P_2(t), s{=}j\omega\} + \left(\frac{V_1P_1^{\,0} + V_2P_2^{\,0}}{V_1 + V_2}\right)\frac{1}{2}\delta(\nu{=}0) \tag{A2}$$

3. Fourier Transform of $\Delta P(t)$. From (A-13)

$$\Delta P(t) = P_1(t) - P_2(t) \rightarrow \Delta P(\omega) = P_1(\omega) - P_2(\omega)$$

$\Delta P(\omega)$ is obtained from $P_1(\omega)$ in (A-1) and $P_2(\omega)$ in (A-2)

$$\Delta P(j\omega) = \frac{(V_1 {P_1}^0 + V_2 {P_2}^0)}{V_2}\left[\sum_{n=0}^{\infty}\left(-\frac{(V_1 - V_2)}{(V_1 + V_2)}\frac{({P_1}^0 - {P_2}^0)}{({P_1}^0 + {P_2}^0)}\right)^n\left(\frac{n\alpha}{n^2\alpha^2 + \omega^2}\right) + \frac{({P_1}^0 - {P_2}^0)}{({P_1}^0 + {P_2}^0)}\sum_{n=0}^{\infty}\left(-\frac{(V_1 - V_2)}{(V_1 + V_2)}\frac{({P_1}^0 - {P_2}^0)}{({P_1}^0 + {P_2}^0)}\right)^n\left(\frac{(n+1)\alpha}{(n+1)^2\alpha^2 + \omega^2}\right) - j\left[\sum_{n=0}^{\infty}\left(-\frac{(V_1 - V_2)}{(V_1 + V_2)}\frac{({P_1}^0 - {P_2}^0)}{({P_1}^0 + {P_2}^0)}\right)^n\left(\frac{\omega}{n^2\alpha^2 + \omega^2}\right) + \frac{({P_1}^0 - {P_2}^0)}{({P_1}^0 + {P_2}^0)}\sum_{n=0}^{\infty}\left(-\frac{(V_1 - V_2)}{(V_1 + V_2)}\frac{({P_1}^0 - {P_2}^0)}{({P_1}^0 + {P_2}^0)}\right)^n\left(\frac{\omega}{(n+1)^2\alpha^2 + \omega^2}\right)\right] + j\frac{1}{\omega}\right] \quad \text{(A3)}$$

4. Fourier Transform of d*n*/d*t*(*t*). From (4.14), dn/dt(t) can be written as

$$\frac{\mathrm{d}n}{\mathrm{d}t}(t) = K'\left[\frac{\mathrm{e}^{\alpha t}}{(1 + Ce^{\alpha t})^2}\right]$$

$P_2(s)$, the Laplace transform of $P_2(t)$, is obtained by direct integration using the series approximation

$$\frac{1}{\left(1 + \frac{1}{C}\mathrm{e}^{-\alpha t}\right)^2} = \sum_{n=0}^{\infty}\left(\frac{-1}{C}\right)^n (n+1)\mathrm{e}^{-n\alpha t}$$

where $x^0 = 0\ \forall\ x \in R$, and the TF d$n$/d$t$ (ω) by substituting $j\omega$ for s. This yields

$$\frac{\mathrm{d}n}{\mathrm{d}t}(j\omega) = \frac{K'}{C^2}\sum_{n=0}^{\infty}\left(-\frac{1}{C}\right)^n\left[\left(\frac{(n+1)^2\alpha}{(n+1)^2\alpha^2 + \omega^2}\right) + j\left(\frac{-(n+1)\omega}{(n+1)^2\alpha^2 + \omega^2}\right)\right] = \left[\frac{4K_{\mathrm{V}}}{RT}\frac{(V_1 {P_1}^0 + V_2 {P_2}^0)^2}{(V_1 + V_2)^2}\frac{({P_1}^0 - {P_2}^0)}{({P_1}^0 + {P_2}^0)}\right] \sum_{n=0}^{\infty}\left[-\frac{(V_1 - V_2)}{(V_1 + V_2)}\frac{({P_1}^0 - {P_2}^0)}{({P_1}^0 + {P_2}^0)}\right]^n\left[\left(\frac{(n+1)^2\alpha}{(n+1)^2\alpha^2 + \omega^2}\right) + j\left(\frac{-(n+1)\omega}{(n+1)^2\alpha^2 + \omega^2}\right)\right] \quad \text{(A4)}$$

References and Notes

(1) Fernandes, T. R. C.; Chen, F.; Carvalho, M. *Int. J. Hydrogen Energy* **2005**, *30*, 239.
(2) Libowitz, G. G.; Hayes, H. F.; Gibb, T. R. P. *J. Phys. Chem.* **1958**, *62*, 76.
(3) Van Vucht, J. H. N.; Kuijpers, F. A.; Bruning, H. C. A. M. *Philips Res. Rep.* **1970**, *25*, 133.
(4) Sandrock, G.; Thomas, G. IEA/DOC/SNL on-line hydride database. *Appl. Phys. A* **2001**, *72*, 153.
(5) Schlapbach, L.; Züttel, A. *Nature* **2001**, *414*, 353.
(6) Luo, W.; Gross, K. J. *J. Alloys Compd.* **2004**, *385*, 224.
(7) Hosoda, H.; Tabaru, T.; Semboshi, S.; Hanada, S. *J. Alloys Compd.* **1998**, *281*, 268.
(8) Urretavizcaya, G.; Fuster, V.; Castro, F. J. *Rev. Sci. Instrum.* **2005**, *76*, 3902.
(9) Dantzer, P.; Millet, P. *Rev. Sci. Instrum.* **2000**, *71*, 142.
(10) Castro, E. B.; Real, S. G.; Bonesi, A.; Visintin, A.; Triaca, W. E. *Electrochim. Acta* **2004**, *49*, 3879.
(11) Millet, P. *Electrochem. Commun.* **2005**, *7*, 40.
(12) Flanagan, T. B.; Clewly, J. D. *J. Less-Common Met.* **1982**, *83*, 127.
(13) Fourier, J. In *Théorie analytique de la chaleur*; Gabay, J., Ed.; Paris, 1985.
(14) Angström, A. J. *Ann. Phys.* (*Weinheim, Ger.*) **1861**, *114*, 513.
(15) Naphthali, L. M.; Polinski, L. M. *J. Phys. Chem.* **1963**, *67*, 369.
(16) Yasuda, Y. *J. Phys. Chem.* **1976**, *80*, 1867.
(17) Gray, E. Mac A. *J. Alloys Compd.* **1992**, *408*, 49.
(18) Millet, P.; Dantzer, P. *J. Alloys Compd.* **1997**, *253*, 542.
(19) Millet, P.; Dantzer, P. *J. Alloys Compd.* **2002**, *330*, 476.
(20) Collet-Lacoste, J. R. *Electrochim. Acta* **2004**, *49*, 4967.
(21) Caï, H.; Millet, P.; Dantzer, P. *J. Alloys Compd.* **1995**, *231*, 427.
(22) Press, W. H. *Numerical Recipes, the Art of Scientific Computing*; Cambridge University Press: Cambridge, 1986.